Full length article

Buckling analysis of subsea pipeline with integral buckle arrestor using vector form intrinsic finite thin shell element

Yang Yu [a,b], Zhenmian Li [a,b,*], Jianxing Yu [a,b], Leige Xu [c], Mingren Zhao [a,b], Yupeng Cui [a,b], Han Wu [d], Qinghao Duan [a,b]

[a] State Key Laboratory of Hydraulic Engineering Simulation and Safety, Tianjin University, Tianjin 300072, China
[b] Tianjin Key Laboratory of Port and Ocean Engineering, Tianjin University, Tianjin 300072, China
[c] School of Civil Engineering and Communication, North China University of Water Resources and Electric Power, Henan, 450045, China
[d] Key Laboratory for Mechanics in Fluid Solid Coupling Systems, Institute of Mechanics, Chinese Academy of Sciences, Beijing 100190, China

A B S T R A C T

Buckling damage is one of the biggest safety issues for subsea pipelines. Buckling behaviors of the subsea pipeline with integral buckle arrestors under external pressure are studied experimentally and numerically herein. Pressure chamber tests of four full-sized pipeline with identical thickness and different diameters are presented. An emerging vector form intrinsic finite element method (VFIFE) is introduced to simulate the whole buckling process both in dynamic and quasi-static cases, including local collapse, propagation, buckling prevention, and crossover. Numerical schemes for multifold nonlinearities and multithreaded computation are proposed and tested. Results of experiments and numerical simulations, as well as computations of the traditional finite element method and DNV specifications, are compared. Thusly it is indicated that the VFIFE model can accurately (within ± 1.5%) predict the buckling loads that initiate local collapse, propagation and crossover, and simulate the dynamic and quasi-static buckling modes for pipelines with practical range of diameter-to-thickness ratios greater than 20. For thick parts where integral arrestor with diameter-to-thickness ratios smaller than 20 located, the VFIFE thin shell element may underestimate the structural strength about 8.0%. The VFIFE can directly simulate the pipeline buckling behavior without special processing for the iterative calculation and the stiffness matrix convergence, and achieve the parallel efficiency over 90% for a common computer (12 threads, 4G RAM). Thus, the VFIFE can provide a new, practical and universal analytic strategy for subsea pipeline buckling analysis.

1. Introduction

Subsea pipelines are exposed to a risk of collapse due to the ambient external pressure. Design specifications, DNV-OS-F101 [1] and API-RP-1111 [2], indicate that subsea pipelines endure only external pressure in the empty waiting state during installation, maintenance, and operation. Moreover, local collapse under external pressure may propagate at high speed and has the potential of destroying the whole line since the pressure to maintain the buckling failure mode along the pipeline, called the propagation pressure, is usually less than the collapse pressure. The buckling of the subsea pipeline will lead to transportation failure and even an oil spill, causing catastrophic losses to the large-scale offshore operations and marine ecology [3,4]. Thus, it is essential to evaluate the collapse strength and analyze the buckling propagation of subsea pipelines.

After nearly one hundred years of research, collapse experiment and its theory on the cylindrical shell under external pressure has

been conducted systematically. Considerable researches ranged from single-walled pipes (Khalipasha and Albermani [3]; Kyriakides and Corona [6]; Yu et al. [7]; Fan et al. [8]) to the pipe-in-pipe system (Karampour et al. [9]; Gong [10]; Alrsai et al. [11]). The most representative work can be found in the research done by Kyriakides's team [6]. They conducted a series of pipeline collapse tests and developed numerical methods considering both geometric and material nonlinearities in the large collapse deformation. Recently, Yu et al. [7,12–16] also conducted a series of reduced-scale and full-scale pipeline tests and revealed the influence of the diameter-to-thickness ratio, ovality, yield strength, corrosion defects for pipeline collapse. Shortly after the discovery of the pipeline buckling propagation phenomenon, the research on buckle arrestors started and three typical types of buckle arrestors have been proposed: integral arrestor, spiral arrestor, slip-on arrestor and welded arrestor [17,18]. Within these arrestors, the cost-effective and excellent performance of the integral arrestor has been highly valued, especially for increasing prosperous deep-water exploration and

---

1-Sealing Hatch, 2-Watertight transducer, 3-Main Chamber body, 4-Exhaust Valve, 5-Water Inlet, 6-Hatch Cover, 7-Pipe, 8-Drain Outlet, 9-Pressure Release Valve.

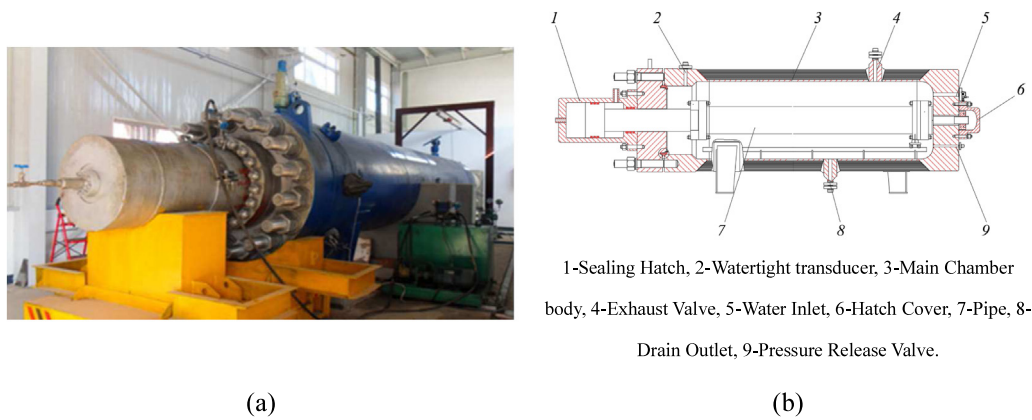(a)   (b)

Fig. 1. Full-size pressure chamber in Tianjin University. (a) Picture of the pressure chamber, (b) Schematic diagram of the pressure chamber.

Table 1
Difference between the FEM and VFIFE [5].

	FEM	VFIFE
Discretization method	Finite elements.	Finite mass particles and their connections.
Computational process	Specific techniques for nonlinear and discontinuous problems.	Directly solution and available intervention in boundary conditions.
Pure deformation	Indirect extraction by derivation.	Direct extraction by translation and rotation.
Stiffness matrix	Global matrix assembled by element matrices.	None.
Ultimate principle	Weak form. Variation principle for holistic structure.	Strong form. Newton's law for each mass particle.

the improved submarine welding technology. Park and Kyriakides [19] conducted a large number of integral arrestor tests with different diameter-to-thickness ratios of pipelines. Netto et al. [20,21] and Lee et al. [22] carried out the dynamic crossover test of the integral arrestor and simulated the dynamic crossover under vacuum conditions. Similar results can also be found in the work of Toscano and Mantovano [23].

Different numerical discretization methods are developed for more accurate pipe structure analysis, especially practical simulation of collapse, propagation and buckle crossover behaviors. Early in 1997, Tassoulas et al. [24] summarized many useful numerical discretization methods for a pipe of uniform thickness. Li Tianyu [25] developed a pipe element for a pipe structure with variable wall thickness and analyzed complicated problems with geometrical nonlinearity well. More effectively and universally, commercial finite element method (FEM) software products [26] such as ANSYS, ABAQUS, and ADINA have been successfully used and proved feasible and reliable. One of the major challenges in such FEM simulation is the possible computation failure caused by the structural nonlinearities, including the material nonlinearity, large deformation, and the contact condition. A successful try of solution to this challenge is to adopt a revision strategy with the help of calculation skills, such as gradually relaxing the basic theoretical assumptions according to the needs of specific behaviors or replacement of calculation modules during iterations [27]. Hereof, the author seeks to develop a newer and simpler analytic strategy for buckling simulation of the subsea pipelines by introducing a newer numerical method, called the vector form intrinsic finite element (VFIFE).

The VFIFE is a new type of finite element method proposed in recent years [5,28,29]. Different from mathematical function description and partial differential equation in the FEM's framework, the VFIFE is based on the basic principles of Newtonian mechanics and uses mass points to describe the physical quantities, such as force, torque, displacement, velocity and acceleration. As illustrated in Table 1, the VFIFE can avoid computing failure due to the ill-conditioned matrix and has great advantages in dealing with discontinuous or nonlinear problems, such as large deformation, large displacements, elastoplasticity, collapse and collision. Up to now, various elements such as beam [30], membrane [31], plate and thin shell [32,33] have been developed. For thin shell elements, Wu [32] established the basic theory of triangular

thin-shell elements and verified its accuracy and reliability in the nonlinear analysis of overall large displacement, large deflection, nonlinear material, and collision contact. In the field of ocean engineering, VFIFE related applications are mainly the beam elements and the use of shell element is rare. It is mainly used in offshore platform dynamic analysis [34], platform-ship collision analysis [35], subsea pipeline mechanics analysis [36], marine riser dynamic analysis [37,38] and other aspects. Especially, local buckling behavior of the subsea pipeline studied by the VFIFE has not been reported.

In this paper, the VFIFE thin shell element is introduced to the complicate problem of subsea pipeline buckling behaviors, including the whole simulation of the collapse, propagation, and crossover. In Section 2, four sets of full-scale experiments are presented with identical thickness and different diameters. Then, the basic theory of the VFIFE shell elements and numerical schemes for multifold nonlinearities are presented and tested in Section 3.1. The VFIFE model of a subsea pipeline with an integral buckle arrestor is proposed in Section 3.2. Section 4 details the experimental results as well as numerical results of the dynamic and quasi-static cases. Discussion about the feasibility and reliability of the simulation is presented in Section 5. Section 6 lists the conclusions of the study along with the further research directions.

2. Experimental test

The pressure chamber [12] shown in Fig. 1 is used to perform pipeline buckling experiments. The chamber includes one main chamber body with 1.0 m internal diameter, sealing hatch and hatch cover. There is a watertight transducer, an exhaust valve, a water inlet, a drain outlet, and a pressure release valve. The chamber can hold an 8.0 m long pipe and has a pressure capacity of 43.00 MPa.

Two sets of pipes are selected with different diameters of 325 mm and 406 mm and the same thickness of 10 mm. Two pipes marked as F1 and F3 are prepared for local collapse and buckling propagation tests. The other two marked as F2 and F4 for buckling propagation and crossover tests. Especially, for F2 and F4, an ovality of about $\Delta_1 = 8.0\%$ is preset near one end of the pipe to induce the local collapse. Details of the four pipes are listed in Table 2.

The experimental procedure of pressure tests for full-size pipes is shown in Fig. 2. The procedure mainly includes pretreatment, equipment and sample installation, pressure test, pressure relief and
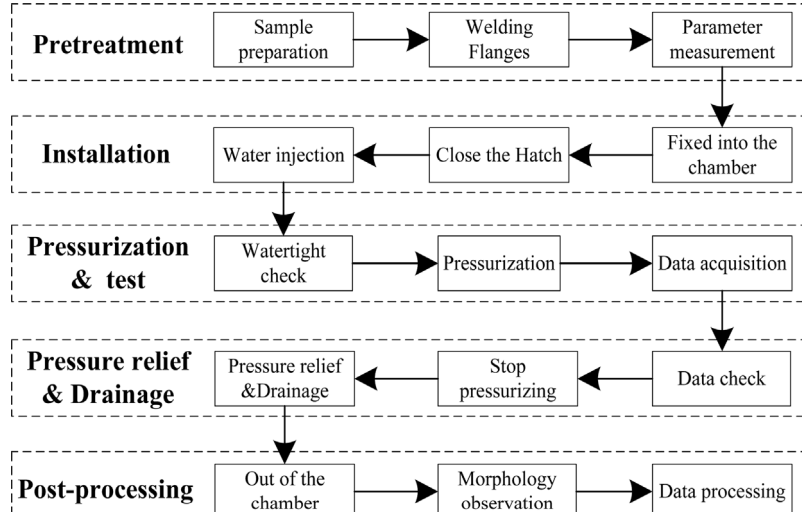
Fig. 2. Experimental procedure of pressure test for full-size pipes.

Table 2
Geometry parameters of pipelines tested.

No.	D, mm	t, mm	Δ_0, %	Δ_1, %	L_a, mm	L_u, m	L_d, m	h, mm
F1	325	10	0.06	–	–	4.00	4.00	–
F2				8.0	160	3.92	3.92	20
F3	406	10	0.05	–	–	4.00	4.00	–
F4				8.0	200	3.90	3.90	20

Table 3
Geometry parameters of pipelines tested.

No.	E, GPa	μ	A_{C-S}, MPa	B_{C-S}, MPa	n_{C-S}
F1	2.06	0.3	448.05	427.80	0.3108
F2					
F3	2.07	0.3	447.72	520.72	0.5237
F4					

drainage, and post-processing. The pretreatment includes sample preparation, flange welding at both ends and measurement of main parameters of the samples. Then, the pipes will be sent into the chamber by a crane and fixed in the chamber by flanges. After shutting down the hatches, the chamber will be filled with water and watertight check is carried out before pressurization using a high-pressure water pump. During pressurization, the maximum loading speed is 2.0 MPa/min and the measurement accuracy of pressure sensors is ± 0.2%. According to the change of water pressure, it can be clearly judged whether pipeline buckling occurs by tracking pressure changes within the chamber. After the pressurization is completed, the pressure will be relieved and the water will be drained. Finally, the test sample will be taken out to observe the morphology. Due to the slow water injection, the loading method is quasi-static and all measured critical pressures are quasi-static buckling loads. It should be noted that more attention is paid to the minimum hydrostatic pressure that initiates or maintains buckling propagation after the local collapse in theoretical research and engineering applications although pipeline buckling is a dynamic process. Therefore, the quasi-static load measured is valuable and the strain rate effects can be ignored.

Sample pieces for material testing are obtained from the test pipes by the slow wire cutting method. Then the quasi-static tensile test method is used to measure the material parameters. The broken pieces and the stress–strain curves are shown respectively in Fig. 3(a) and (b). The nonlinear Cowper–Symonds (C–S) material model [39] is used to describe the constitutive relationship of materials, as shown in the following equation:

$$\sigma_p = A_{C-S} + B_{C-S}\varepsilon_p^{n_{C-S}} \left[1 + \left(\frac{\dot{\varepsilon}}{C} \right)^{1/p} \right] \tag{1}$$

where σ_p is the dynamic yield stress; A_{C-S} is the quasi-static yield stress, and n_{C-S} are the strain hardening parameters under quasi-static conditions; C and p are the material parameters related to the strain rate effect. As mentioned above, the strain rate effect was neglected and imperative material parameters were gained by fitting experimental curves (see Table 3).

3. Methods and materials

This section firstly introduces briefly the basic theory of the VFIFE thin shell element. Then, numerical schemes for multifold nonlinearities including geometrical, material and boundary nonlinearities are proposed. A FORTRAN procedure of the VFIFE 3D shell element is developed and validated. The Open Multi-Processing (Open MP) techniques is introduced and tested. Finally, a specific VFIFE model is proposed for subsea pipeline. Refer to literatures [32,33] for details about the VFIFE method.

3.1. Basic theory of VFIFE thin shell element

3.1.1. Nodal motion equations

In the VFIFE method, the structure will be modeled by a set of mass particles and massless elements, as shown in Fig. 1. Mass particles are used to describe the kinematics and dynamics of the structure and elements constrain spatial motion of those mass particles. During the time $t_0 \leq t \leq t_k$, the motion of an arbitrary particle i in shell can be illustrated by a motion trajectory which is identified by a series of time instants t_j, $j = 0, 1, 2, \ldots, n-1, n, \ldots, k$. The trajectory segment of $t_{n-1} \leq t \leq t_n$ is referred to as a path element of particle i. The motion of a particle along a path element can be directly formulated by Newton's law, namely

$$\begin{cases} \boldsymbol{M}_i \ddot{\boldsymbol{x}}_i + \alpha \boldsymbol{M}_i \dot{\boldsymbol{x}}_i = \boldsymbol{F}_i \\ \boldsymbol{I}_i \ddot{\boldsymbol{\theta}}_i + \beta \boldsymbol{I}_i \dot{\boldsymbol{\theta}}_i = \boldsymbol{F}_{\theta,i} \end{cases} \tag{2}$$

where $\boldsymbol{M}_i$ and $\boldsymbol{I}_i$ are the mass and mass moment of inertia, $\boldsymbol{x}_i$ is the translational displacement, and $\boldsymbol{\theta}_i$, $\boldsymbol{F}_i$ and $\boldsymbol{F}_{\theta,i}$ denote the rotational angle, applied force vectors and moment vectors of particle i. α and β are the damping parameters for translation and rotation, usually $\alpha = \beta$.

Using the central different method, Eq. (2) can be rewrote as

$$\begin{cases} \boldsymbol{x}_i^{n+1} = c_1 \boldsymbol{M}_i^{-1} \boldsymbol{F}_i^n (\Delta t)^2 + 2c_1 \boldsymbol{x}_i^n - c_2 \boldsymbol{x}_i^{n-1} \\ \boldsymbol{\theta}_i^{n+1} = c_1 \boldsymbol{I}_i^{-1} \boldsymbol{F}_{\theta,i}^n (\Delta t)^2 + 2c_1 \boldsymbol{\theta}_i^n - c_2 \boldsymbol{\theta}_i^{n-1} \end{cases} \tag{3}$$
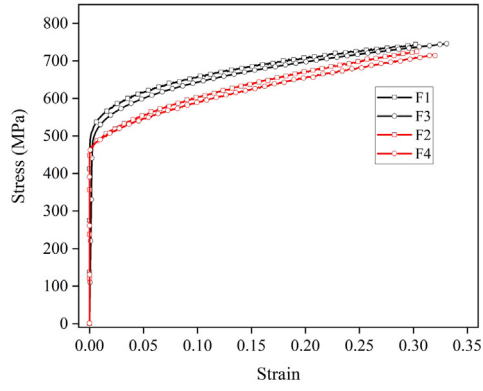
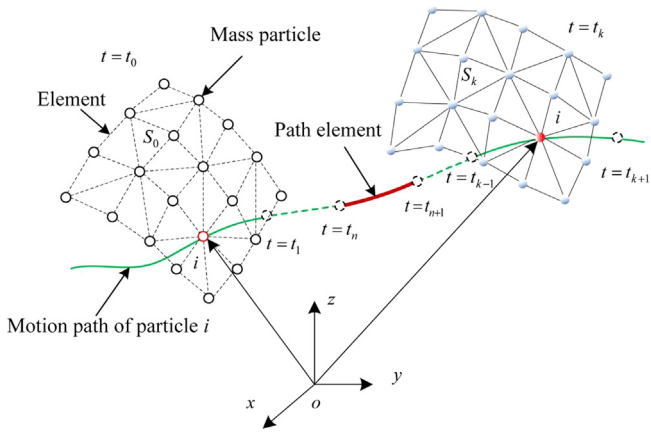Fig. 3. The quasi-static tensile test. (a) Pieces after test, (b) Stress–strain curves.

Fig. 4. Motion of particle i in a solid described by mass points.

Fig. 5. Space movement of a triangular shell element.

where the superscripts, n-1, n, and n+1, denote the time steps, Δt the time step, c_1 and c_2 are damping parameters.

3.1.2. Pure deformation calculation

The motions solved by Eq. (3) include rigid body motions and pure deformations. In vector form analysis, pure deformations are essential for s evaluation of trains within the elements. During time iteration, pure deformations for each element are calculated by the inverse motion method [32,33] and then used to gain the internal force vectors and moment vectors.

As shown in Fig. 5, a triangular shell element (defined by three mass particles, (m_a, m_b, m_c)) moves from $(m_a^{n-1}, m_b^{n-1}, m_c^{n-1})$ to (m_a^n, m_b^n, m_c^n) along a path element, say $t_{n-1} \leq t \leq t_n$. The position of these particles changes from $(x_i^{n-1}, \theta_i^{n-1})$ to (x_i^n, θ_i^n) so that the increment is $(\Delta x_i, \theta x_i) = (x_i^n - x_i^{n-1}, \theta_i^n - \theta_i^{n-1})$, $i = a, b, c$. Take m_a as the reference point, the inverse motion travels through $(m_a^n, m_b^n, m_c^n) \rightarrow (m_a', m_b', m_c') \rightarrow (m_a'', m_b'', m_c'') \rightarrow (m_a''', m_b''', m_c''') \rightarrow (m_a^{n-1}, m_b^{n-1}, m_c^{n-1})$ after imposing the reverse translation, the reverse out-plane rotation, and the reverse in-plane rotation.

After the reverse translation with respect to m_a, these mass particles arrives (m_a', m_b', m_c'), and its position is

$$\begin{cases} x_i' = x_i'^n - \Delta x_a' \\ \theta_i' = \theta_i^n \end{cases}, i = a, b, c \tag{4}$$

Then the mass particles should return to the same plane of (m_a^n, m_b^n, m_c^n) by the reverse out-plane rotation. The out-plane rotation angle and
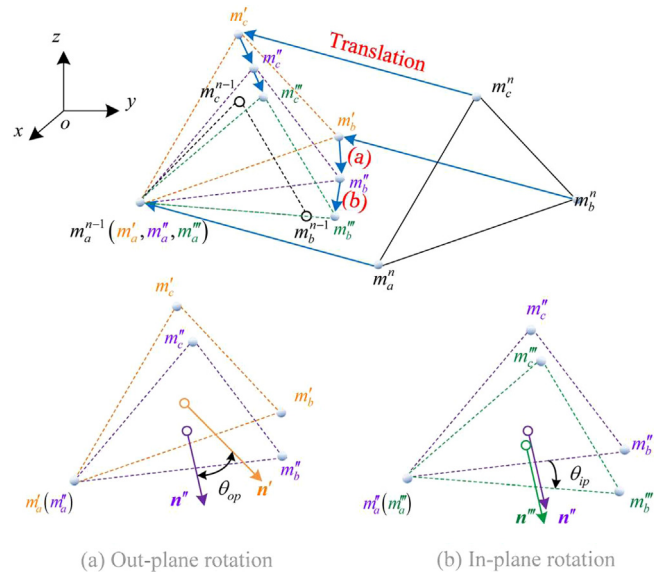
direction vector are

$$\begin{cases} \theta_{op} = \cos^{-1}\left(\dfrac{\mathbf{n}' \cdot \mathbf{n}''}{|\mathbf{n}'|\,|\mathbf{n}''|}\right), \theta_{op} \in [0, \pi] \\ \mathbf{n}_{op} = \dfrac{\mathbf{n}' \times \mathbf{n}''}{|\mathbf{n}'|\,|\mathbf{n}''|} = [l_{op}, m_{op}, n_{op}]^T \end{cases} \tag{5}$$

where $\mathbf{n}'$ and $\mathbf{n}''$ are the normal vectors of (m_a^n, m_b^n, m_c^n) and $(m_a^{n-1}, m_b^{n-1}, m_c^{n-1})$.

Therefore, the position of (m_a'', m_b'', m_c'') is

$$\begin{cases} x_i'' = x_i' + \mathbf{R}_{op}^*\left(-\theta_{op}\right) \cdot \left(x_i' - x_a'\right) \\ \theta_i'' = \theta_i' - \theta_{op} \cdot \mathbf{n}_{op} \end{cases}, i = a, b, c \tag{6}$$

where

$$\mathbf{R}_{op}^*\left(-\theta_{op}\right) = \left[1 - \cos\left(-\theta_{op}\right)\right] \mathbf{A}_{op}^2 + \sin\left(-\theta_{op}\right) \mathbf{A}_{op},$$

$$\mathbf{A}_{op} = \begin{bmatrix} 0 & -n_{op} & m_{op} \\ n_{op} & 0 & l_{op} \\ m_{op} & l_{op} & 0 \end{bmatrix}.$$
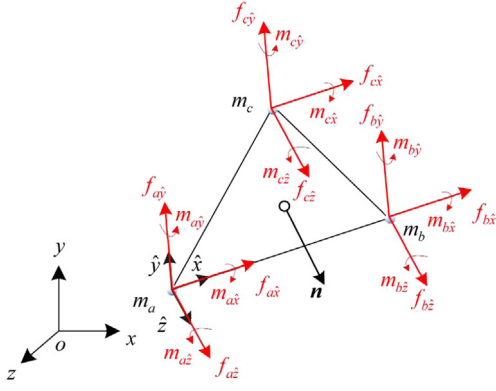
Fig. 6. Nodal forces and moments within an element.

The in-plane rotation angle and direction vector are

$$
\begin{cases}
\theta_{ip} = sign^{-1} \left[\left(\boldsymbol{x}_a'' - \boldsymbol{x}_i'' \right) \times \left(\boldsymbol{x}_a^{n-1} - \boldsymbol{x}_i^{n-1} \right) \cdot \boldsymbol{n}'' \right] \\
\quad \times \left| \cos^{-1} \left[\dfrac{\left(\boldsymbol{x}_a'' - \boldsymbol{x}_i'' \right) \times \left(\boldsymbol{x}_a^{n-1} - \boldsymbol{x}_i^{n-1} \right)}{\left| \boldsymbol{x}_a'' - \boldsymbol{x}_i'' \right| \left| \boldsymbol{x}_a^{n-1} - \boldsymbol{x}_i^{n-1} \right|} \right] \right|, \theta_{ip} \in [-\pi, \pi] \\
\boldsymbol{n}_{ip} = \boldsymbol{n}'' = \left[l_{ip}, m_{ip}, n_{ip} \right]^T
\end{cases}
\tag{7}
$$

Therefore, the configuration of $\left(m_a''', m_b''', m_c''' \right)$ is

$$
\begin{cases}
\boldsymbol{x}_i''' = \boldsymbol{x}_i'' + \boldsymbol{R}_{ip}^* \left(-\theta_{ip} \right) \cdot \left(\boldsymbol{x}_a'' - \boldsymbol{x}_i'' \right) \\
\boldsymbol{\theta}_i''' = \boldsymbol{\theta}_i'' - \theta_{ip} \cdot \boldsymbol{n}_{ip}
\end{cases}, i = a, b, c
\tag{8}
$$

Where $\boldsymbol{R}_{ip}^* \left(-\theta_{ip} \right)$ and $\boldsymbol{A}_{ip}$ are similar to $\boldsymbol{R}_{op}^* \left(-\theta_{op} \right)$ and $\boldsymbol{A}_{op}$ respectively.

After above inverse motion, the pure deformation of the element can be written as

$$
\begin{cases}
\Delta \boldsymbol{x}_i^p = \boldsymbol{x}_i''' - \boldsymbol{x}_i^{n-1} \\
\Delta \boldsymbol{\theta}_i^p = \boldsymbol{\theta}_i''' - \boldsymbol{\theta}_i^{n-1}
\end{cases}, i = a, b, c
\tag{9}
$$

3.1.3. Internal force calculation

As shown in Fig. 6, the pure deformation presented in Eq. (9) can be descried within the element by a transform operator $\boldsymbol{A}_{gl}$ from the global coordinate $oxyz$ to the local coordinate $\hat{o}\hat{x}\hat{y}\hat{z}$ as

$$
\begin{cases}
\Delta \hat{\boldsymbol{x}}_i^p = \boldsymbol{A}_{gl} \Delta \boldsymbol{x}_i^p \\
\Delta \hat{\boldsymbol{\theta}}_i^p = \boldsymbol{A}_{gl} \Delta \boldsymbol{\theta}_i^p
\end{cases}, i = a, b, c
\tag{10}
$$

Actually, the thin shell element with the local coordinate is a plane shell element after inverse motion. For a plane shell element, its displacement vector can be expressed after ignoring zero component as

$$
\hat{\boldsymbol{U}} = \left\{ \hat{y}_b, \hat{x}_c, \hat{y}_c, \hat{\theta}_{a\hat{x}}, \hat{\theta}_{a\hat{y}}, \hat{\theta}_{b\hat{x}}, \hat{\theta}_{b\hat{y}}, \hat{\theta}_{c\hat{x}}, \hat{\theta}_{c\hat{y}} \right\}^T
\tag{11}
$$

Then, the internal force of the particles are solved based on the following virtual work equation.

$$
\delta \hat{\boldsymbol{U}} \cdot \hat{\boldsymbol{f}} = \int_S \delta \left(\Delta \hat{\varepsilon} \right) \cdot \sigma \, dS
\tag{12}
$$

where $\hat{\varepsilon}$ and $\hat{\sigma}$ are the strain vector and stress vector, $\hat{\boldsymbol{f}}$ is the nodal forces and moments vector, $\hat{\boldsymbol{f}} = \left\{ \hat{f}_{b\hat{y}}, \hat{f}_{c\hat{x}}, \hat{f}_{c\hat{y}}, \hat{m}_{a\hat{x}}, \hat{m}_{a\hat{y}}, \hat{m}_{b\hat{x}}, \hat{m}_{b\hat{y}}, \hat{m}_{c\hat{x}}, \hat{m}_{c\hat{y}} \right\}^T$.

For an arbitrary shell element, the internal forces and moments under the local coordinate can be gained by solving the following static equilibrium equations

$$
\sum \hat{F}_{\hat{x}} = 0, \quad \sum \hat{f}_{i\hat{x}} = 0, \quad i = a, b, c
\tag{13}
$$

$$
\sum \hat{F}_{\hat{y}} = 0, \quad \sum \hat{f}_{i\hat{y}} = 0, \quad i = a, b, c
\tag{14}
$$

$$
\sum \hat{F}_{\hat{z}} = 0, \quad \sum \hat{f}_{i\hat{z}} = 0, \quad i = a, b, c
\tag{15}
$$

$$
\sum \hat{M}_x = 0, \quad \hat{m}_{a\hat{x}} + \hat{m}_{b\hat{x}} + \hat{m}_{c\hat{x}} + \hat{f}_{c\hat{z}} \hat{y}_c = 0
\tag{16}
$$

$$
\sum \hat{M}_y = 0, \quad \hat{m}_{a\hat{y}} + \hat{m}_{b\hat{y}} + \hat{m}_{c\hat{y}} - \hat{f}_{b\hat{z}} \hat{x}_b - \hat{f}_{c\hat{z}} \hat{x}_c = 0
\tag{17}
$$

$$
\sum \hat{M}_z = 0, \quad \hat{f}_{b\hat{y}} \hat{x}_b + \hat{f}_{b\hat{x}} \hat{x}_b + \hat{f}_{c\hat{x}} \hat{y}_c - \hat{f}_{c\hat{y}} \hat{x}_c = 0
\tag{18}
$$

Finally, the internal forces and moments $\boldsymbol{f}_{\text{int}}$ will be used for Eq. (1) after conversion of the two coordinate systems, namely

$$
\boldsymbol{f}_{\text{int}} = \left(\boldsymbol{R}_{ip}^* + \boldsymbol{I} \right)^T \left(\boldsymbol{R}_{op}^* + \boldsymbol{I} \right)^T \boldsymbol{A}_{gl}^T \hat{\boldsymbol{f}}_i, i = a, b, c
\tag{19}
$$

3.2. Numerical schemes for multifold nonlinearities

3.2.1. Geometrical nonlinearities

As mentioned in Section 3.1, VFIFE is based on the basic principles of Newtonian Mechanics and uses mass points to describe the physical quantities such as force, torque, displacement, velocity and acceleration. Since the geometric and positional changes of the structure are included and naturally displayed in the displacement of the particles, no special correction processing is required for possible large displacement or large deformation.

3.2.2. Material nonlinearities

For common materials, such as steel, the stress–strain relationship will be nonlinear when the external load reaches a certain value, called plasticity. Moreover, there is irreversible inelastic deformation in the plastic part of the structure. To deal with such material nonlinearities, VFIFE needs an elastoplastic correction to obtain the accurate stress and strain state of the structure. The correction is executed after the pure deformation calculation (see Section 3.1.2) and then used for the calculation of internal forces (see Section 3.1.3).

As shown in Fig. 7, the elastoplastic correction mainly includes three steps, elastic prediction, elastoplastic judgment and plastic correction. The process is as follows

Step 1 Elastic prediction. Calculate strain increment $\Delta \varepsilon$ using the pure deformation presented in Eq. (10). Assuming that the material is in an elastic state, calculate the stress increment $\Delta \overline{\sigma}$ and stress at next timestep $\overline{\sigma}^{n+1} = \sigma^{n+1} + \Delta \overline{\sigma}$.

Step 2 Elastoplastic judgment. Calculate the values of the yield function, $F \left(\overline{\sigma}^{n+1}, \varepsilon_p^n \right)$ and $F \left(\sigma^{n+1}, \varepsilon_p^n \right)$, and determine the elasticity factor m.

- If $F \left(\overline{\sigma}^{n+1}, \varepsilon_p^n \right) \leq 0$, the time step is elastic loading or elastic unloading from plasticity. For this case, there is none plastic strain and $m = 1$.
- If $F \left(\overline{\sigma}^{n+1}, \varepsilon_p^n \right) > 0$ and $F \left(\sigma^{n+1}, \varepsilon_p^n \right) < 0$, the time step is in transition state from elastic to plastic. For this case, the elasticity factor m is calculated using Von Mises yield criterion [27] and given as

$$
m = \left(-a_1 + \sqrt{a_1^2 - 4a_0 a_2} \right) / 2a_2
\tag{20}
$$

Where $a_0 = F \left(\sigma^n, \varepsilon_p^n \right)$, $a_1 = \left({}^n \boldsymbol{S}, \Delta \hat{\boldsymbol{x}}^p \right)^T {}^n \overline{\boldsymbol{S}}$, $a_2 = 0.5 \Delta \overline{\boldsymbol{S}}^T \overline{\boldsymbol{S}}$, $\boldsymbol{S}$ and $\Delta \boldsymbol{S}$ are deviatoric stress and its increment.

- If $F \left(\overline{\sigma}^{n+1}, \varepsilon_p^n \right) > 0$ and $F \left(\sigma^n, \varepsilon_p^n \right) = 0$, the time step is plastic loading from plasticity. For this case, there is none elastic strain and $m = 0$.

Step 3 Plastic correction. Calculate plastic stress increment $\Delta \sigma_p$ using the C–S material model (see Eq. (1)). Update the plastic strain ε_p^{n+1} and stress σ^{n+1} for next time steps.

The above elastoplastic correction is often used in traditional FEM calculations, and it is also effective for VFIFE. The difference is that VFIFE does not need to calculate the elastoplastic element stiffness matrix (usually higher order than the elastic stiffness matrix and deformation-dependent) and assemble overall stiffness matrix after the elastoplastic correction. This can reduce the computational workload and avoid the trouble of matrix solving.
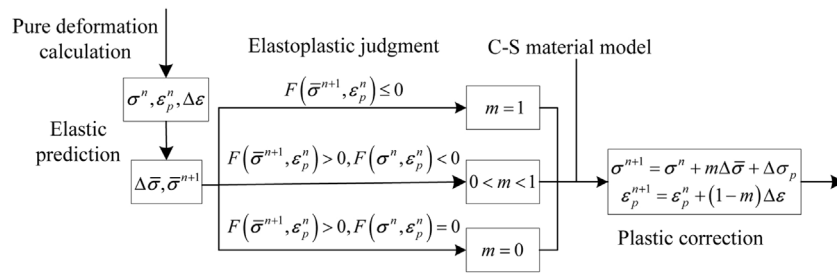
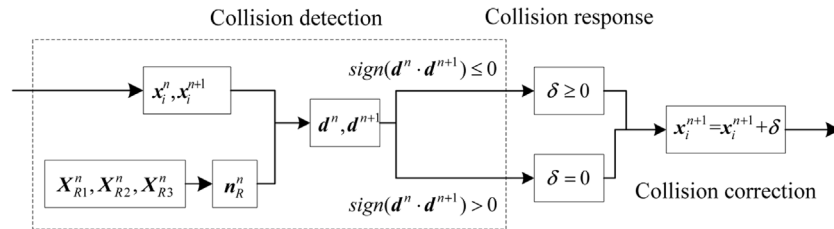**Fig. 7.** Elastoplastic correction of the plastic strain and stress for integration points.

Fig. 8. Collision correction for each particle.

3.2.3. Boundary nonlinearities

The boundary nonlinearities discussed in this paper are mainly two problems. One is that the magnitude and direction of the external force on the force boundary depends on the deformation, and the other is the collision problem. For the former case, boundary detection is required. Each triangular shell element (see Fig. 4) will be traverse and their normal vectors as well as areas will be calculated based on the coordinates of their three particles. Then, the pressure can be accurately loaded on the constantly changing surface.

For the collision problem, collision detection and collision response processing are needed. The correction procedure for each particle collided with the rigid surface is shown Fig. 8, described as

Step 1 Collision detection. Calculate the normal vector n_R^n using the coordinates of three nodes of a certain element of rigid surface. Calculate the distances from the particle to the rigid surface at time step n and $n+1$, marked as d^n and d^{n+1}. Determine whether there is a collision by the value of $sign(d^n \cdot d^{n+1})$.

Step 2 Collision response. Calculate the displacement correction δ.

- If $sign(d^n \cdot d^{n+1}) > 0$, none collision occurs and $\delta = 0$.
- If $sign(d^n \cdot d^{n+1}) \leq 0$, collision occurs and $\delta \geq 0$. This paper considers the smooth collision and the penalty function method [40] is used to calculate δ.

Step 2 Collision correction. Correct the particle displacement using δ.

The above collision correction is similar to the explicit solution of boundary nonlinear problems in traditional FEM [27,40]. The explicit solution is popular with respect the implicit solution in FEM since it uses the equivalent nodal force vector to avoid unsymmetrical stiffness matrix and adjoint calculation problem. But because of this, the explicit solution is inapplicable for buckling simulation as the stiffness matrix does change during boundary nonlinear processing. For VFIFE, the above explicit algorithm is convenient and effective because VFIFE itself is an explicit method. There is none stiffness matrix for VFIFE and above simple operations are all based on the coordinates of the particles.

3.3. Computations implementation and validation

As described in Eq. (3), the governing equations of mass particles are two sets of second-order differential equations. During each time step, the internal force calculation is performed after pure deformation

is gained by the inverse motion method. As shown in Fig. 9, the main computational flow is listed in the following two main modules:

- Particle Motion Calculation. Compute the motions (x_i^{n+1} and θ_i^{n+1}) by Eq. (3).
- Element Force Evaluation. Pure deformation is obtained by the inverse motion method and separated for the thin membrane elements and thin plate elements (see Eq. (8)). Then, the internal force integrations are carried out based on the virtual work principle (see Eq. (12)) and elastoplastic correction (see Section 3.2.2). The internal force vectors are assembled by the linear superposition of the two different elements. The external force vectors are loaded after boundary detection (see Section 3.2.3).

The basic calculation of VFIFE is the particle traversal and element traversal. Therefore, the VFIFE is convenient for entire structural behaviors tracking and fine for massively parallel computation [41]. In this study, the computations are implemented by Fortran programs, optimized by the Open Multi-Processing (Open MP) techniques [42] and processed by Matlab programs for visualization.

Before modeling and analyzing the subsea pipeline, a short cylindrical shell under axial compression [33] is tested as a verification case. The cylindrical shell structure with an axial length 0.5 m, a constant thickness 2.0 mm, and a middle surface radius 0.1 m, is meshed by 40×32 particles (40 in the circumference and 32 in the length). The Young's modulus is 201 GPa and the Poisson's ratio is 0.3. The bottom side of the structure is fixed and the top side only allows the axial displacement. The loading speed on the top side is 40 m/s and the time step is set as 1.0×10^{-6} s. The calculation is executed using 12 threads. The computer configuration is as follows: Intel(R) Core (TM) i7-8700 CPU @3.20 GHz and 4.0 GB RAM. As shown in Fig. 10(a), the first three buckling behaviors were simulated and compared with the published result [33] as well as the result of ABAQUS. It is obviously that the loading–shortening curves are much the same and the first three buckling loads had a margin of error of 0.84%, 9.57% and −0.22% with respect to ABAQUS. The error of the second buckling load may be caused by the strong form requirement of VFIFE. Fig. 10(b) shows that the significant speedup has been obtained when using multithreads, and the parallel implementation efficiency preponderates over 90% ($T_1 = 334.35$ s for one thread).
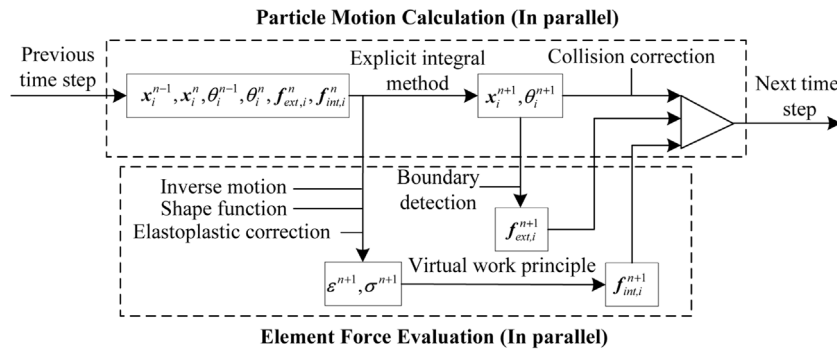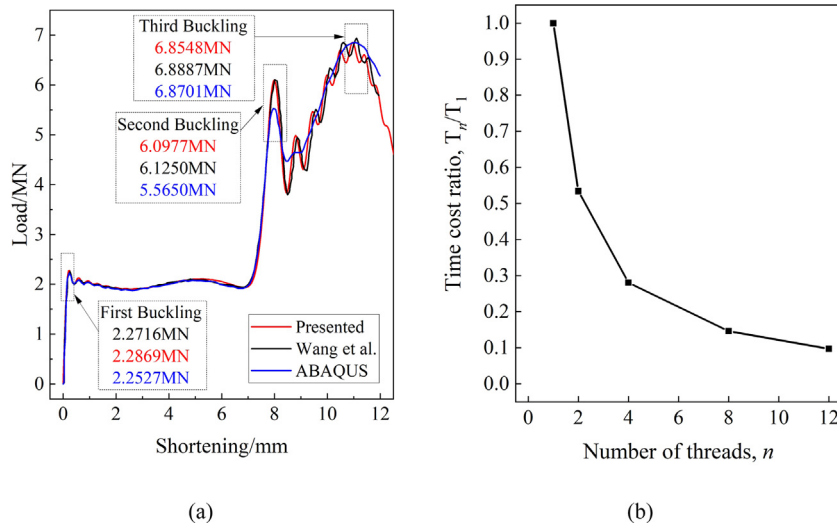
Fig. 9. Calculation flow of the VFIFE shell model.

(a)

(b)

Fig. 10. Cylindrical shell under axial compression. (a) Result validation, (b) Parallel implementation efficiency.

3.4. VFIFE model of subsea pipeline

Fig. 11 shows the VFIFE model of a subsea pipeline with an integral arrestor. Triangulation is used for mass particles and elements mesh generation. The pipeline is divided into three parts: the upstream section, the arrestor, and the downstream section. For the above three parts, their length and thickness are L_u, L_a, L_d and t, t and h. The diameter of the pipeline is D and its initial ovality is Δ_0. As there are two symmetry axes for an ellipse, only a quarter of the model is needed. In the coordinate system $oxyz$, plane oyz and oxz are symmetry planes where mass particles located are subject to symmetric boundary conditions. Mass particles with $z = L_u + L_a + L_d$ are rigidly fixed while mass particles with $z = 0$ are also set symmetrical about the plane oxy to induce local collapse.

The above boundary conditions can simplify the model and improve computational efficiency. The expected result is that local collapse occurs in the cross-section at $z = 0$ and propagates along the upstream pipeline until encounters the arrestor. Then, the collapse will travel across the arrestor and propagate within the downstream pipeline. When the local collapse occurs, the upper and lower wall of the pipeline may collide and will directly affect the subsequent buckling propagation and crossover behaviors. Therefore, the planes oxz and oyz should be first defined as rigid planes to prevent penetrations. This approach is often used in ABAQUS simulation [14,16,26]. Accurately, the influence of wall thickness should be considered so that the radial bending displacement of all parts of the pipeline is limited within $(D-t)/2$.

4. Results

4.1. Experimental results

Fig. 12 shows the pressure–time curves of the four tests. The red curves are the pre-selected plans with the maximum loading speed (2 MPa/min) and limited maximum pressures, 15 MPa for two collapse and propagation tests and 10 MPa for two propagation and crossover tests. At first the actual water pressures in the chamber rose slowly and then increased rapidly with a maximum speed about 2 MPa/min. For Fig. 12(a), the collapse pressure could be determined when the water pressure dropped dramatically during the pressurization process. This is due to the local collapse of the pipeline which leads to a sudden increase in the water volume within the chamber. It is first stage of pipeline buckling and can also be found in Fig. 12(b). Then, pressurization continued to induce propagation. Different from the first pressurization process, the water pressure would keep a stable value for some time after a slight increase. It is the second stage of the tests and the stable value is the propagation pressure. During this stage, the local collapse traveled along the pipeline. When the collapse reached the end of the pipeline, the water pressure would rise again since there was no more deformations. For Fig. 12(b), the water pressure experienced a significant rise and fall again after propagation. The reason is that the propagation was firstly stopped by the arrestor. Crossover happened in the second rise and fall of water pressure. Therefore, the second pressure peak is the crossover pressure of the integral arrestor.

As shown in Fig. 12(a), the collapse pressures of F1 and F2 are 11.59 and 6.23 MPa while their propagation pressures are 2.67 and 1.57 MPa. The main reason for the differences in their anti-pressure capabilities
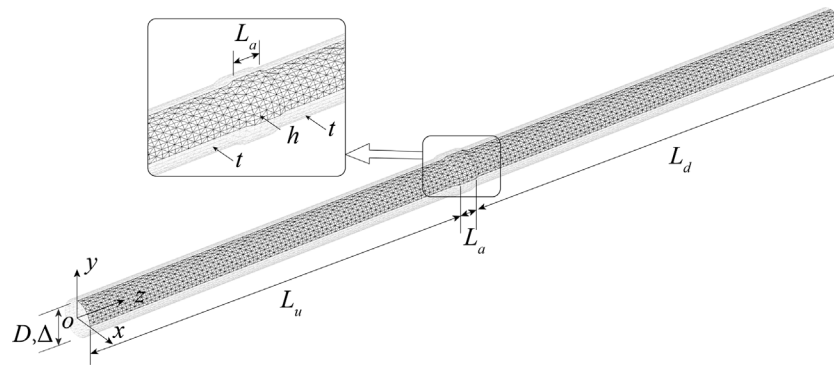
Fig. 11. VFIFE model of a subsea pipeline with an integral buckle arrestor.

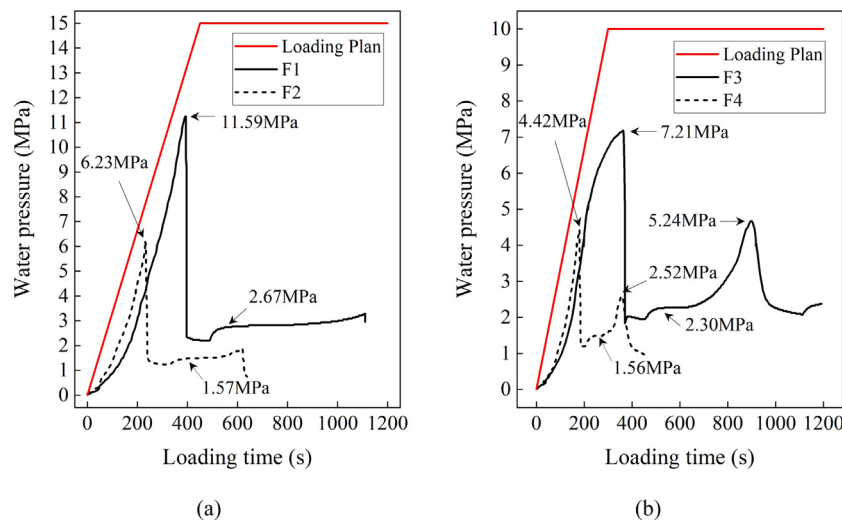|	
(a)	(b)

Fig. 12. Water pressure–time curves. (a) Collapse and propagation tests, (b) Propagation and crossover tests.

is the diameter–thickness ratio. Likewise, the collapse, propagation and crossover pressures of F3 and F4 can be found in Fig. 12(b). The collapse pressures of F3 and F4 went an apparent decline because of the preset large ovality. Due to the limited space within the chamber, the water pressure rose faster during pressurization and dropped to a lower level when collapse and crossover happened for pipelines with larger diameters (F2 and F4).

The morphology of pipelines after tests are shown in Fig. 13. After the collapse and propagation tests, pipelines F1 and F2 were flattened overall. As often occurs [19,20], the cross-sectional shape of the collapsed pipelines is dumbbell-like and it travels along the pipeline after propagation. In Fig. 13(b), the dumbbell-like deformation went through the arrestors and the whole structure was crushed. It can be found that pipelines with a larger diameter–thickness ratio had a more pronounced arc in its cross-sections. The reason is that lower water pressure after collapse does not sufficiently flatten the tube.

4.2. Numerical results

4.2.1. Dynamic buckling

According to the basic theory presented in Section 3.1, the VFIFE is an explicit dynamic method. For pipeline buckling analysis, determination of quasi-static loading speed, just as the experimental pressure speed, is necessary for computing the minimum critical load. On the other hand, to reduce computational time, the speed of quasi-static loading should be set as large as possible.

As shown in Fig. 14, specific nodal displacements under different loading speeds are monitored. The selected particles are located at both ends of the cross-section $z = 0$ and their initial coordinates are $\left(D_{\max}/2, 0, 0\right)$ and $\left(D_{\min}/2, 0, 0\right)$. Six loading speeds, $P_v = 50.0, 40.0, 30.0, 20.0, 15.0, 10.0$ MPa/s, were tested. As shown in Fig. 14(a), the nodal displacements would suddenly change when the external pressure reached a certain value. Using the Budiansky–Roth (B–R) dynamic buckling criterion [43], the buckling pressure can be determined when a small increase in loads results in a huge change in the structural responses. The collapse pressures with different loading speeds are 11.70, 11.64, 11.60, 11.58, 11.56, and 11.55 MPa, shown by red square dots and dotted lines in Fig. 14(a). Therefore, the pressure speed for quasi-static loading was identified as 10 MPa/s. Another two particles located in the midsection of the arrestor were selected and their nodal displacements history is drawn on Fig. 14(b). Similar changes can also be found and indicated that crossover appeared shortly after the local collapse and propagation in the upstream pipeline.

The deformation and Von Mises Stress distribution under different pressures are shown in Fig. 15. At the beginning of the collapse (①~④), the deformations are not evident. Because of the larger projected areas on the plane oxy, stress around the ends of the short axis is higher than that around the ends of the long axis (see ② in Fig. 15, 5.00 MPa). Then, the stress around the ends of the long axis would rise after the stresses around the ends of the short axis reached to the critical yield surface. And the lower stress occurred in the middle ground between the two ends of the short and long axis (see ③ in Fig. 15, 10.00 MPa). Along with the increase of the pressure, the stress distribution was trending collapse: the stresses around the ends of both the long and short axis reached to critical yield surface (see ④ in Fig. 15, 11.55MPa). In this state, a small increase in pressure lead to local large deformation and cross-sections near $z = 0$ became flat (see ⑤ in Fig. 15, 11.61 MPa).
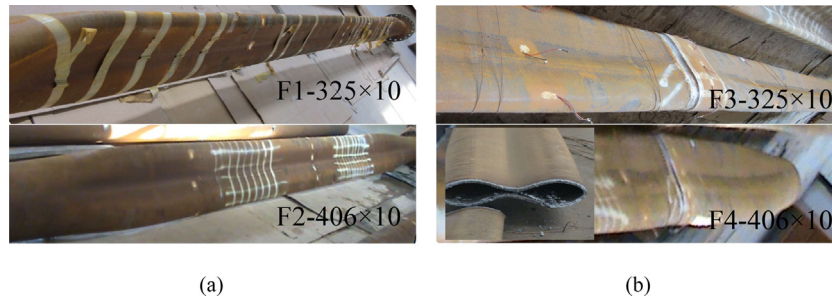
Fig. 13. Pipe morphology after tests. (a) Collapse and propagation tests, (b) Propagation and crossover tests.
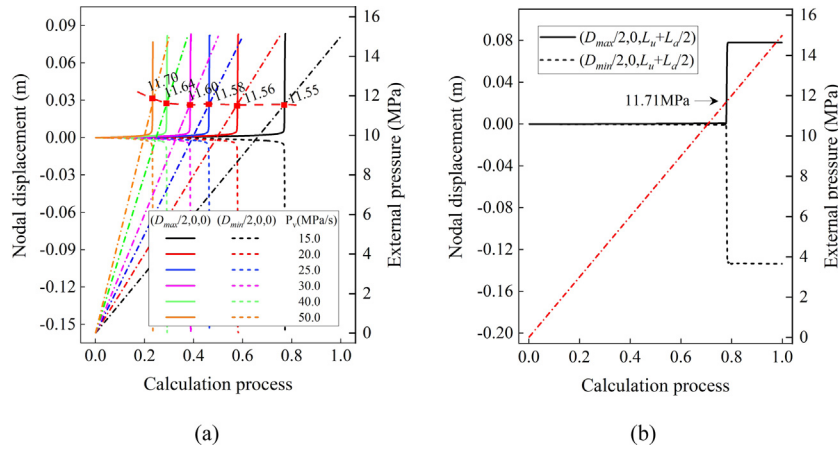

Fig. 14. Time history curves of nodal displacements and external pressure. (a) $\left(D_{\max}/2, 0, 0\right)$ and $\left(D_{\min}/2, 0, 0\right)$, (b) $\left(D_{\max}/2, 0, L_u + L_a/2\right)$ and $\left(D_{\min}/2, 0, L_u + L_a/2\right)$.
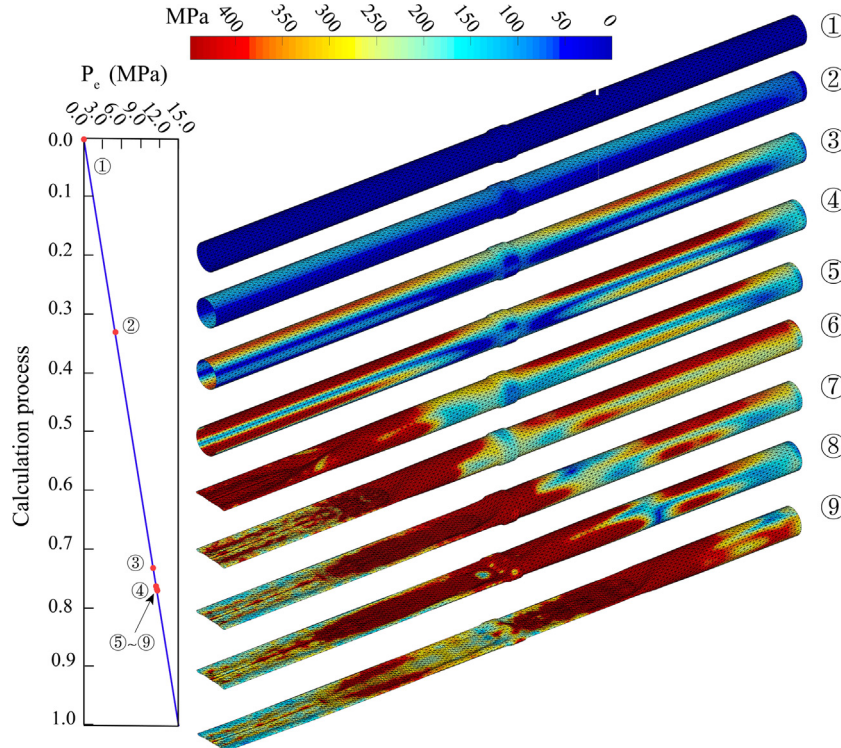

Fig. 15. Deformation and Von Mises Stress distribution of pipeline A in different external pressure. ①0.00 MPa, ②5.00 MPa, ③10.00 MPa, ④11.55 MPa, ⑤11.61 MPa, ⑥11.64 MPa, ⑦11.70 MPa, ⑧11.73 MPa, ⑨11.79 MPa.

When the pressure continued to increase slightly, the local collapse spread throughout the pipeline at a very fast speed. Materials became plastic when the cross-sections were collapsing and would return to a low-stress level after propagation. It should be noted that the buckling
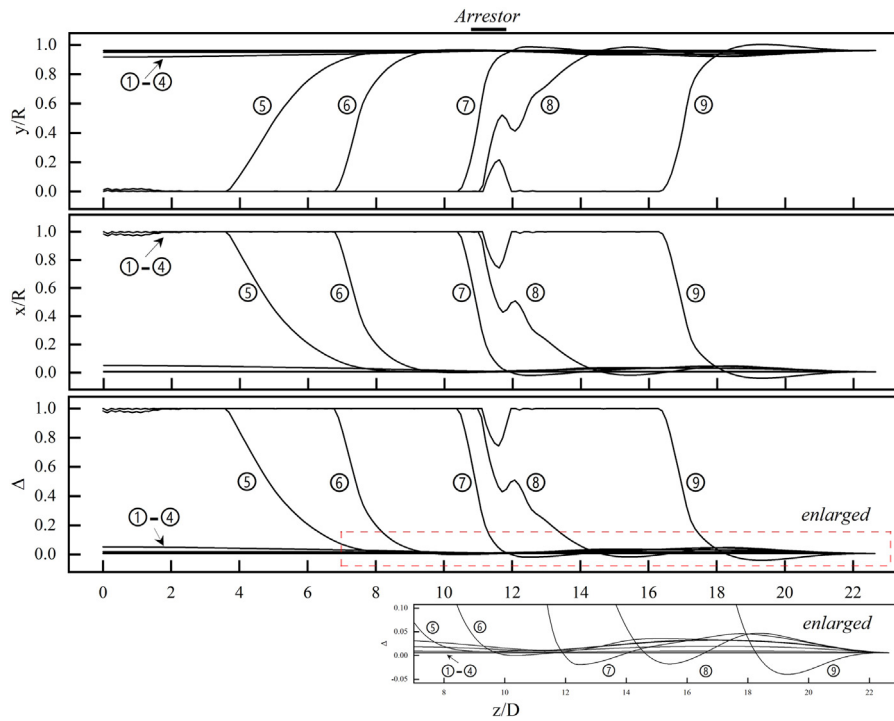
Fig. 16. A sequence of calculated contours of mass particles in the dynamic case. ①0.00 MPa, ②5.00 MPa, ③10.00 MPa, ④11.55 MPa, ⑤11.61 MPa, ⑥11.64 MPa, ⑦11.70 MPa, ⑧11.73 MPa, ⑨11.79 MPa.
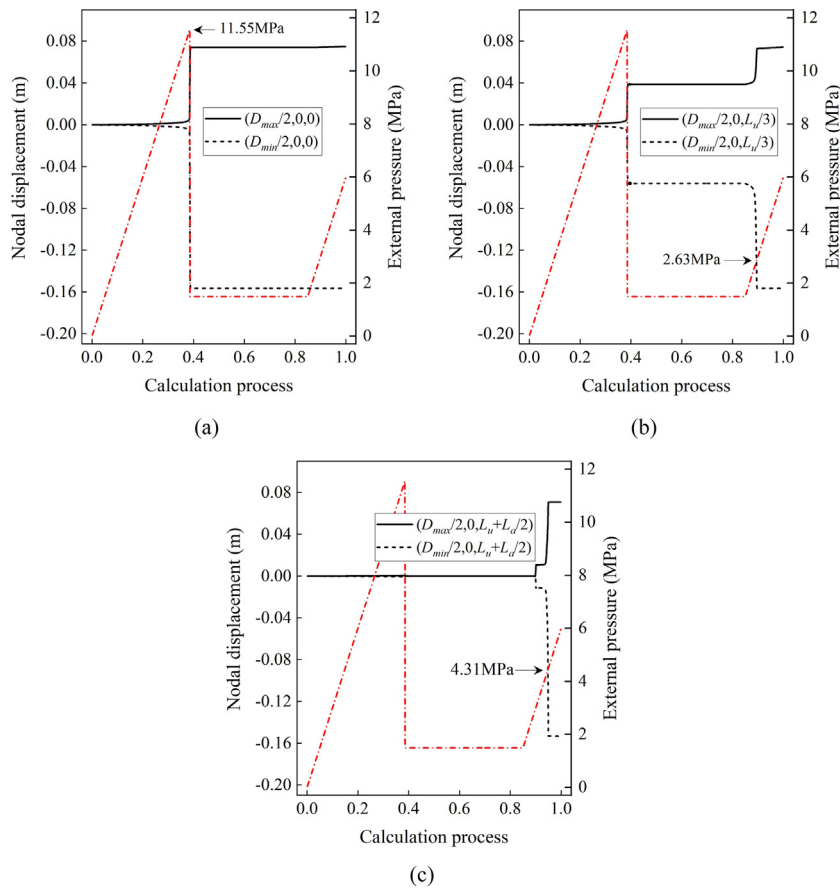

Fig. 17. Nodal displacement history pipeline A. (a) Buckling, (b) Propagation, and (c) crossover.

behavior is called "dynamic buckling" since the external pressure keeps with regardless of the large deformation of the pipeline [20,21].

Further analysis of the deformed configurations and the cross-section ovalities are as follows. The contours shown in Fig. 16 from
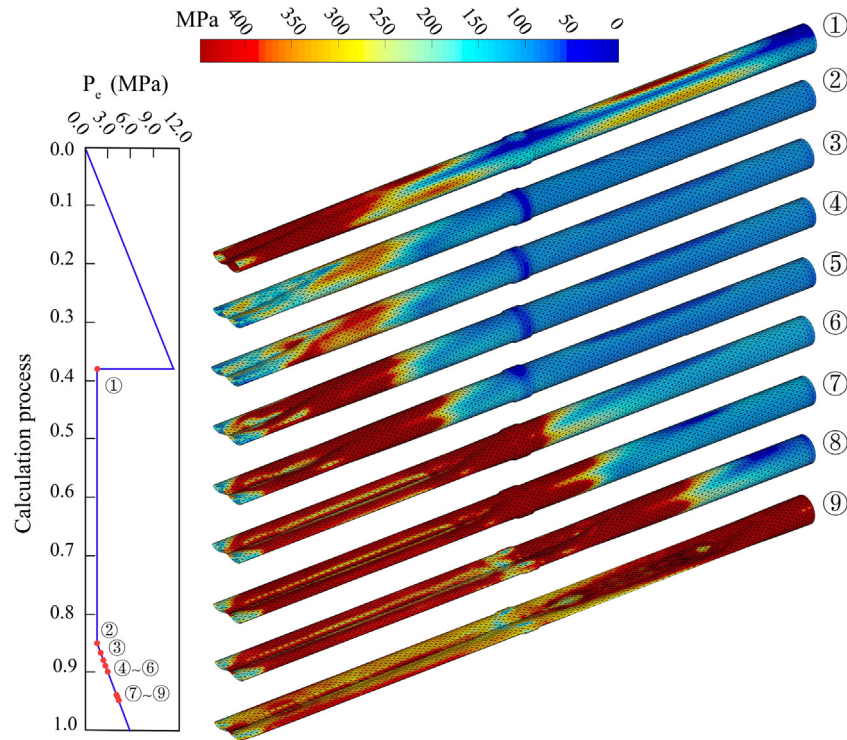
Fig. 18. Deformation and Von Mises Stress distribution of pipeline A in different external pressure. ①1.50 MPa, ②1.50 MPa, ③2.00 MPa, ④2.63 MPa, ⑤2.76 MPa, ⑥3.00 MPa, ⑦4.31 MPa, ⑧4.35 MPa, ⑨4.40 MPa.

top to bottom are deformed configurations of the mass particles at $x = 0$ and $y = 0$, and the cross-section ovalities. At the beginning of the collapse stage (①∼④), particles at $x = 0$ and $y = 0$ occurred certain radial displacement which decreased with the increase of z coordinate. When collapse occurred, the particle at ($x = 0$, $z = 0$) reached the symmetry plane $y = 0$ and put the near particles in a downward motion. Because of the arrestor, the profiles at $x = 0$ and $y = 0$ were becoming steeper (⑤∼⑦) when the collapse propagated in the upstream pipe. Then, crossover happened and propagation continued (⑧∼⑨). The propagation length is defined by the nearest distance (along z direction) between the particle which just reaches the symmetry plane $x = 0$ and the particle which is about to collapse. Obviously, the propagation length will be reduced when propagation approaches the arrestor as well as propagation continues in the downstream pipeline.

Another important feature of the dynamic buckling behavior is that inverse ovalities occur in the downstream pipeline. As shown in Fig. 16, particles at $x = 0$ and $y = 0$ in the downstream pipeline moved in the direction against that of nodes in the upstream pipeline (⑦∼⑨). The reason for this feature is that upstream propagation leads to axial compression and results in a radial expansion in the downstream.

4.2.2. Quasi-static buckling

Another procedure for quasi-static buckling behaviors simulation is described in this section. In present calculations, an additional subroutine for collapse identification and monotonical pressure change was added. Once the collapse at $z = 0$ happened, the external pressure would be adjusted to a lower value, like the turning point observed in tests (see Fig. 12). Moreover, there is a cooling-off stage to relieve the influences of inertial force and stress wave. Then, the pressure would increase again for propagation and crossover simulation.

As shown in Fig. 17, displacements of mass particles at $\left(D_{\max}/2, 0, 0\right)$ and $\left(D_{\min}/2, 0, 0\right)$ changed suddenly when the pressure curve dropped from 11.55 to 1.50 MPa. Different from that shown in Fig. 14(a), particle at $\left(D_{\max}/2, 0, 0\right)$ did not move adequately when particle at $\left(D_{\min}/2, 0, 0\right)$ reached the symmetry plane $y = 0$. It means that the cross section at $z = 0$ had not been sufficiently flatted due to the synchronous

pressure change. Despite that, the deformation was mainly plastic and did not bounce back. The other two particles at $\left(D_{\max}/2, 0, L_u/3\right)$ and $\left(D_{\min}/2, 0, L_u/3\right)$ were monitored and there were two sudden changes in their displacement curves. The first one occurred when collapse happened and the cross section was not flatted. The second one happened when propagation began and the cross section became the same shape as that at $z = 0$ (see Fig. 17(a)). Two particles located in the midsection of the arrestor ($\left(D_{\max}/2, L_u + L_a/2\right)$ and $\left(D_{\min}/2, L_u + L_a/2\right)$) were selected for crossover identification and their displacements history was drawn on Fig.17(c). They experienced unconspicuous elastic deformation in the collapse stage and returned to their original position when the external pressure dropped. The particles moved a limited but plastic distance when propagation approached and achieved similar displacements after crossover (see Fig. 17(a) and (b)). The propagation and crossover pressures are eventually identified to be 2.63 and 4.31 MPa.

The sequences of the deformation and Von Mises Stress distribution after the collapse are shown in Fig. 18. At the beginning of the cooling-off stage (①), the stress in the slope near $z = 0$ was very high and narrow high-stress regions were also found in the downstream pipeline. After the cooling-off stage, the stress distribution would become smooth and steady (see ② in Fig. 18). Residual stresses are mainly distributed near the cross-section at $z = L_u/3$. The lowest stress region was in the arrestor and the downstream pipeline was also in low-stress level. Particle at $\left(D_{\min}/2, 0, 0\right)$ reached the symmetry plane and the cross-section at $z = 0$ was dumbbell-like. Then, the stress around the slope was rising along with the increase of the external pressure (③∼④). Propagation happened when the pipe-segment in the slope was all in plastic as shown by ④ in Fig. 18. In this state, a small increase in external pressure lead to dumbbell-like deformation traveled along the upstream pipeline (⑤∼⑥). The propagation would be stopped by the arrestor (⑥) and the crossover happened until the external pressure reached the crossover pressure (⑦). Then, the propagation continued and the downstream pipe became flat (⑧∼⑨).

Similar contours as Fig. 16 are shown in Fig. 19 for the quasi-static case. In the cooling-off stage (①∼②), particles at $x = 0$ and $y = 0$
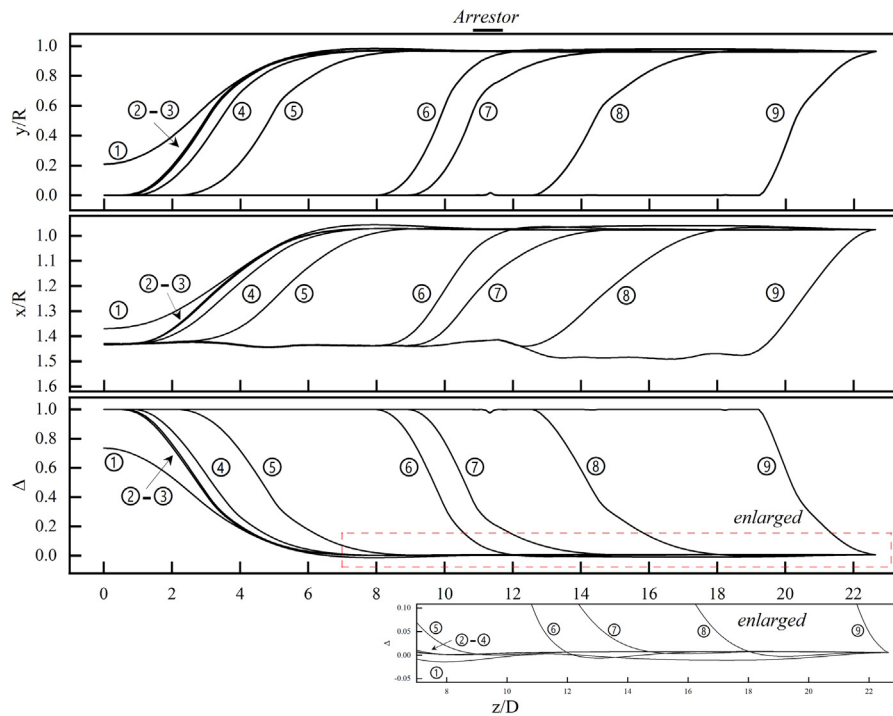
Fig. 19. A sequence of calculated contours of mass particles in the quasi-static case. ①1.50 MPa, ②1.50 MPa, ③2.00 MPa, ④2.63 MPa, ⑤2.76 MPa, ⑥3.00 MPa, ⑦4.31 MPa, ⑧4.35 MPa, ⑨4.40 MPa.

would move continuously after the pressure drop due to their inertia force and the former would reach the plane $y = 0$. At the beginning of the second pressurization process, the position of these particles did not change obviously (②∼③). When the external pressure approached the propagation pressure, the displacements of particles in the slope would become large and local collapse propagated in the upstream pipe (④∼⑥). When the external pressure approached the crossover pressure, the arrestor became flatten and propagation marched (⑦∼⑨) in the downstream pipe. Different from the dynamic case, the axial compression on the downstream was smaller and none obvious inverse ovalities were observed.

One important feature is the different propagation modes in the downstream and upstream pipelines. As shown in Fig. 18, propagation mode in the upstream is a dumbbell-like cross-section while that in the downstream is flat. Moreover, the cross-sections of the arrestor were flatter than that shown in Fig. 16.

5. Discussion

In this paper, an emerging numerical method, VFIFE thin shell element, was introduced to analyze buckling behaviors of the subsea pipeline. Results both in the experiments and numerical calculations in Section 4 proved the effectiveness of the method adopted. The VFIFE model of the subsea pipeline with an integral buckling arrestor in Section 3.4 can achieve whole simulations of collapse, propagation, and crossover.

For the pipeline structure buckling analysis, significant emphasis should be put on its critical pressures, including the collapse pressure, the propagation pressure, and the crossover pressure. Comparison of those critical pressures in different methods, including the experiments shown in Section 2, the VFIFE method shown in Section 3, the FEM (ABAQUS, F3D3 and C3D8I elements) [14,15], and the DNV specifications [1], is listed in Table 4. It is shown that the collapse pressures and propagation pressures obtained by different methods are comparable to each other. The margin of error for these two pressures was within ± 1.5%. The propagation pressure of F2 is lower than other results because of the preset ovality for collapse induction. As for the crossover

Table 4
Comparison of critical pressures in different methods.

Critical pressure (MPa)	No.	Experiment	VFIFE	FEM	DNV
Collapse pressure	F1	11.59	11.55	11.43	11.84
	F2	6.23	6.30	6.34	6.26
Propagation pressure	F1	2.67	2.63	2.56	2.50
	F2	2.30			
	F3	1.57	1.58	1.51	1.43
	F4	1.56			
Crossover pressure	F3	5.24	4.31	4.72	4.68
	F4	2.52	2.62	2.55	2.49

pressure, the value measured in F3 is the maximum while the VFIFE result is the minimum. The reason for a bigger tested crossover pressure of F3 may be the smaller ovality of the arrestor which is welded between two lengths of pipe or the welding quality. Moreover, the error percentages of the VFIFE method are −8.69% and −7.91% with respect to the FEM and DNV specifications. But for F4, the crossover pressures from different methods achieve good agreement. It should be noted that the diameter–thickness ratios of the buckle arrestor for F3 and F4 are 16.25 and 20.3 respectively. For pipe structures, the thin shell structures usually refer to those whose diameter–thickness ratios are larger than 20 while the rest are thick shell structures. The thin shell elements used in this study ignore the shear bearing capacity of the thick shell and lead to a certain calculation error of the crossover pressure. In this sense, it is necessary to develop thick shell elements or solid elements for thick pipes or segments. Even so, the thin shell element is accurate enough for thin pipelines which are common in offshore oil and gas exploitation.

Through the comparison between the calculated and tested morphology of pipelines, two different buckling modes can be simulated by the VFIFE method. Kyriakides [19,20] also reported the two different buckling modes respectively in quasi-static propagation and dynamic propagation (see also Ref. [21, Fig. 4]). For the quasi-static propagation, the crown points of the collapsed cross-section behind the front are in contact essentially along an axial line. In the dynamic case,

the tube behind the buckle is essentially flattened by the much higher ambient pressure and by the inertial forces. As shown in Figs. 15 and 18, the dynamic case has a much sharper buckle profile (the length is approximate 4*D*) than the quasi-static case (the length is approximate 6*D*). A new phenomenon found in the quasi-static case is that the propagation configuration in the downstream pipeline after crossover is similar to that in the dynamic case. This is because there is none pressure drop when the crossover happened and the subsequent process is a dynamic case.

The reverse ovalities adjacent to the profile should be also be focused on. As shown in the enlarged subplots in Figs. 16 and 19, inverse ovalities are found in the front region near collapse. In the dynamic buckling case, reverse ovalization is seen to be more obvious as the propagation passes through the arrestor and approaches to the fixed ends. The maximum value of the reverse ovality is approximately 3.98% and the length is approximately 1.72*D*. As for the quasi-static case, the maximum value of the reverse ovalities are quite smaller (approximately 0.60%) but the length is longer (approximately 2.09*D*). Axial compression during propagation is the cause for such reverse ovalities and also leaded obvious wrinkle near $z = 0$ in the dynamic case.

As per the VFIFE thin shell elements, the whole buckling process of the pipeline with an integral buckle arrestor can be directly simulated in line with the actual situation. The VFIFE has the advantage of not requiring special calculation processing for such tough problems like singular stiffness matrices and can track the entire behavior by inquiring the information of mass particles directly. Thus, the VFIFE can act as a new and universal analytic strategy for subsea pipelines buckling simulation and guide its design, construction, and in-situ analysis. It must be mentioned here that in this paper the fluid–solid coupling and the material strain rate are ignored as they are not urgent and major factors for pipeline buckling problem. Further research would be firstly directed at developing solid elements for the thick segments for pipelines and then account for the fluid–solid interaction and more complex material models.

6. Conclusions

In this study, a new procedure was developed based on the VFIFE thin shell element and achieved buckling analysis for a subsea pipeline with an integral buckling arrestor. Full-size tests in the pressure chamber were also carried out to measure the critical pressure values of the collapse, propagation, and crossover process. Comparison of the results of full-size tests, the VFIFE calculation, the FEM calculation, and the DNV specification is presented to prove the accuracy of the proposed method. We also elaborated on the buckling behaviors in two different loading cases, dynamic and quasi-static buckling.

Results proved that the VFIFE thin shell element can simulate the collapse, propagation, buckling prevention, and crossover behavior of subsea pipelines. The VFIFE thin shell elements can accurately (within ± 1.5%) predict critical pressures for different buckling process and simulate the dynamic and quasi-static buckling modes for thin pipelines (diameter–thickness ratios ≥ 20). For thick pipelines (diameter–thickness ratios ≤ 20), the predicted critical loads would be smaller (about - 8.0%) as the thin shell elements ignore the shear bearing capacity of the thick shell. Moreover, the VFIFE method uses Newton's law to achieve strong form description of structure behaviors and solve the structural deformation and internal force directly without complicated computation techniques. Using Open MP technique, the parallel implementation efficiency preponderates over 90% for a common office computer (12 threads, 4G RAM). Therefore, the VFIFE thin shell element can provide a new, practical and universal analysis strategy for subsea pipelines buckling analysis.

It is clear that the VFIFE model of the subsea pipeline has not been fully developed. As the discussion states, the thin shell element may lead to certain errors for thick pipelines or segments. Further research should be focused on the development of thick shell element or solid element for wider and more comprehensive application.

CRediT authorship contribution statement

Yang Yu: Conceptualization, Methodology, Visualization, Investigation, Writing - review & editing, Supervision, Funding acquisition. **Zhenmian Li:** Conceptualization, Methodology, Software, Validation, Writing - original draft, Writing - review & editing. **Jianxing Yu:** Software, Validation, Supervision, Funding acquisition. **Leige Xu:** Methodology. **Mingren Zhao:** Software, Validation, Writing - original draft. **Yupeng Cui:** Writing - original draft. **Han Wu:** Visualization, Investigation, Writing - review & editing. **Qinghao Duan:** Writing - review & editing.

Acknowledgments

Appendix A. Supplementary data

Supplementary material related to this article can be found online at https://doi.org/10.1016/j.tws.2021.107533.

References

[1] DNV OS F 101, DNV-OS-F101: Submarine pipeline systems, DNV OS F101, 2013, https://doi.org/DNV-OS-F101.

[2] The American Petroleum Institute, API RP 1111 4th edition-design, construction, operation, and maintenance of offshore hydrocarbon pipelines (limit state design), 2009, https://doi.org/10.7202/1016404ar.

[3] H. Khalilpasha, F. Albermani, Hyperbaric chamber test of subsea pipelines, Thin-Walled Struct. (2013) https://doi.org/10.1016/j.tws.2013.05.001.

[4] Z. Wang, G.H.M. van der Heijden, Localised lateral buckling of partially embedded subsea pipelines with nonlinear soil resistance, Thin-Walled Struct. (2017) https://doi.org/10.1016/j.tws.2017.05.017.

[5] Lu. Zhe-gang, Yao. Jian, Vector form intrinsic finite element – a new numerical method, Spatial Struct. (2012) https://doi.org/10.13849/j.issn.1006-6578.2012.01.015.

[6] S. Kyriakides, E. Corona, Mechanics of Offshore Pipelines, 2007, https://doi.org/10.1016/B978-0-08-046732-0.X5000-4.

[7] J.X. Yu, Z.Z. Sun, X.X. Liu, Y.X. Zhai, Ring-truss theory on offshore pipelines buckle propagation, Thin-Walled Struct. (2014) https://doi.org/10.1016/j.tws.2014.08.015.

[8] Z. Fan, J. Yu, Z. Sun, H. Wang, Effect of axial length parameters of ovality on the collapse pressure of offshore pipelines, Thin-Walled Struct. (2017) https://doi.org/10.1016/j.tws.2017.02.032.

[9] H. Karampour, F. Albermani, M. Veidt, Buckle interaction in deep subsea pipelines, Thin-Walled Struct. (2013) https://doi.org/10.1016/j.tws.2013.07.003.

[10] S. Gong, X. Wang, T. Zhang, C. Liu, Buckle propagation of sandwich pipes under external pressure, Eng. Struct. (2018) https://doi.org/10.1016/j.engstruct.2018.08.033.

[11] M. Alrsai, H. Karampour, F. Albermani, Numerical study and parametric analysis of the propagation buckling behaviour of subsea pipe-in-pipe systems, Thin-Walled Struct. (2018) https://doi.org/10.1016/j.tws.2018.01.019.

[12] J. Yu, X.X. Liu, Z. Sun, H. Wu, Y. Liu, Y. Zhao, Full-scale pipeline buckling test in hyperbaric chamber, in: Ocean. 2014 - TAIPEI, 2014, https://doi.org/10.1109/OCEANS-TAIPEI.2014.6964459.

[13] W. Ma, J. Yu, Q. Zhou, B. Xie, J. Cao, Z. Li, Nonlinear contact between inner walls of deep sea pipelines in buckling process, J. Ocean Univ. China. (2015) https://doi.org/10.1007/s11802-015-2368-8.

[14] J. xing Yu, J. hui Duan, Z. zhou Sun, Y. Yu, M. ning Wu, The cross-over mechanisms of integral buckle arrestors for offshore pipelines, Appl. Ocean Res. (2017) https://doi.org/10.1016/j.apor.2017.07.016.

[15] H. Wang, Y. Yu, J. Yu, J. Duan, Y. Zhang, Z. Li, C. Wang, Effect of 3D random pitting defects on the collapse pressure of pipe — Part I: Experiment, Thin-Walled Struct. (2018) https://doi.org/10.1016/j.tws.2018.04.015.

[16] H. Wang, Y. Yu, J. Yu, C. Jin, Y. Zhao, Z. Fan, Y. Zhang, Effect of 3D random pitting defects on the collapse pressure of pipe — Part II: Numerical analysis, Thin-Walled Struct. (2018) https://doi.org/10.1016/j.tws.2018.04.014.

[17] T.A. Netto, S.F. Estefen, Buckle arrestors for deepwater pipelines, Mar. Struct. (1996) https://doi.org/10.1016/0951-8339(95)00036-4.

[18] G.D. Hahn, M. She, J.F. Carney, Buckle propagation and arresting in offshore pipelines, Thin-Walled Struct. (1994) https://doi.org/10.1016/0263-8231(94)90021-3.

[19] T.D. Park, S. Kyriakides, On the performance of integral buckle arrestors for offshore pipelines, Int. J. Mech. Sci. (1997) https://doi.org/10.1016/s0020-7403(96)00074-4.

[20] T.A. Netto, S. Kyriakides, Dynamic performance of integral buckle arrestors for offshore pipelines. Part I: experiments, Int. J. Mech. Sci. (2000) https://doi.org/10.1016/S0020-7403(99)00052-1.

[21] T.A. Netto, S. Kyriakides, Dynamic performance of integral buckle arrestors for offshore pipelines. Part II: analysis, Int. J. Mech. Sci. (2000) https://doi.org/10.1016/S0020-7403(99)00053-3.

[22] L.H. Lee, S. Kyriakides, T.A. Netto, Integral buckle arrestors for offshore pipelines: Enhanced design criteria, Int. J. Mech. Sci. (2008) https://doi.org/10.1016/j.ijmecsci.2008.02.008.

[23] R.G. Toscano, L.O. Mantovano, P.M. Amenta, R.F. Charreau, D.H. Johnson, A.P. Assanelli, E.N. Dvorkin, Collapse arrestors for deepwater pipelines, cross-over mechanisms, Comput. Struct. (2008) https://doi.org/10.1016/j.compstruc.2007.07.009.

[24] J.L. Tassoulas, S.A. Karamanos, G.N. Mansour, A.C. Nogueira, Finite element analysis of tube stability in deep water, Comput. Struct. (1997) https://doi.org/10.1016/S0045-7949(96)00175-7.

[25] T. Li, On the formulation of a pipe element for a pipe structure with variable wall thickness, Ocean Eng. (2016) https://doi.org/10.1016/j.oceaneng.2016.03.036.

[26] Q. Bai, Y. Bai, Subsea pipeline design, analysis, and installation, 2014, https://doi.org/10.1016/C2010-0-67706-6.

[27] I.M. Smith, D.V. Griffiths, L. Margetts, Programming the Finite Element Method, fifth ed., 2015, https://doi.org/10.1002/9781119189237.

[28] E.C. Ting, C. Shih, Y.K. Wang, Fundamentals of a vector form intrinsic finite element: Part I. Basic procedure and a plane frame element, J. Mech. (2004) https://doi.org/10.1017/S1727719100003336.

[29] E.C. Ting, C. Shih, Y.K. Wang, Fundamentals of a vector form intrinsic finite element: Part II. Plane solid elements, J. Mech. (2004) https://doi.org/10.1017/S1727719100003348.

[30] Y.F. Duan, S.M. Wang, J.D. Yau, Vector form intrinsic finite element method for analysis of train-bridge interaction problems considering the coach-coupler effect, Int. J. Struct. Stab. Dyn. (2019) https://doi.org/10.1142/S0219455419500147.

[31] Q. Qing, S. Shen, J. Gong, Deflation behavior and related safety assessment of an air-supported membrane structure, Thin-Walled Struct. (2018) https://doi.org/10.1016/j.tws.2018.01.037.

[32] T.Y. Wu, Dynamic nonlinear analysis of shell structures using a vector form intrinsic finite element, Eng. Struct. (2013) https://doi.org/10.1016/j.engstruct.2013.08.009.

[33] X. Wang Y. Zhao, Yang, Collision-contact, crack-fracture and penetration behavior analysis of thin-shell structures based on vector form intrinsic finite element, Jianzhu Jiegou Xuebao/J. Build. Struct. (2016) https://doi.org/10.14006/j.jzjgxb.2016.06.007.

[34] D. Hu, Y. He, W.L. Jin, Vifie-based prediction and strength analysis on upending of spar, in: Proc. Int. Conf. Offshore Mech. Arct. Eng. - OMAE, 2010, https://doi.org/10.1115/OMAE2010-20955.

[35] Z.H. Yao, M.W. Yuan, H.-H. Lee, K.-W. Tseng, P.-Y. Chang, The application of vector form intrinsic finite element method to template offshore structures, Comput. Mech. (2007) https://doi.org/10.1007/978-3-540-75999-7_78.

[36] L. Xu, M. Lin, Numerical study on critical axial forces of upheaval buckling for initially stressed submarine pipelines on uneven seabed, Ocean Eng. (2017) https://doi.org/10.1016/j.oceaneng.2017.09.013.

[37] X. Li, X. Guo, H. Guo, Vector form intrinsic finite element method for nonlinear analysis of three-dimensional marine risers, Ocean Eng. (2018) https://doi.org/10.1016/j.oceaneng.2018.05.009.

[38] H. Wu, X. Zeng, J. Xiao, Y. Yu, X. Dai, J. Yu, Vector form intrinsic finite-element analysis of static and dynamic behavior of deep-sea flexible pipe, Int. J. Nav. Archit. Ocean Eng. (2020) https://doi.org/10.1016/j.ijnaoe.2020.04.003.

[39] M.F. Buchely, A. Maranon, V.V. Silberschmidt, Material model for modeling clay at high strain rates, Int. J. Impact Eng. (2016) https://doi.org/10.1016/j.ijimpeng.2015.11.005.

[40] M. Zang, W. Gao, Z. Lei, A contact algorithm for 3D discrete and finite element contact problems based on penalty function method, Comput. Mech. (2011) https://doi.org/10.1007/s00466-011-0606-5.

[41] Y. Duan, J. Tao, H. Zhang, S. Wang, C. Yun, Real-time hybrid simulation based on vector form intrinsic finite element and field programmable gate array, Struct. Control Heal. Monit. (2019) https://doi.org/10.1002/stc.2277.

[42] The OpenMP API specification for parallel programming. https://www.openmp.org/ (Accessed on 7th September 2020).

[43] J.W. Hutchinson, B. Budiansky, Dynamic buckling estimates, AIAA J. (1966) https://doi.org/10.2514/3.3468.